

# Time Dependent Filamentation and Stimulated Brillouin Forward Scattering in Inertial Confinement Fusion Plasmas

Andrew J. Schmitt\*

Plasma Physics Division, Naval Research Laboratory, Washington DC 20375

Bedros B. Afeyan

Institute for Laser Science and Applications and Department of Applied Science,  
University of California, Davis-Livermore, Livermore CA 94551

15 November 1997

## Abstract

Numerical simulations of the temporal evolution of laser light filamentation and stimulated Brillouin forward scattering (SBFS) in plasmas, under conditions that are relevant to laser fusion, are presented and analyzed. Long term unsteady behavior of filaments is observed to be the norm. Temporal and spatial incoherence due to filamentation and SBFS are impressed upon time-independent incident laser beams. The bandwidth and angular divergence imposed upon the beam increase with the strength of the interaction. In addition, the spectrum of the transmitted light is redshifted by an amount that increases with the interaction strength. Spectral analysis of the transmitted light reveals that SBFS plays a role in the generation of the observed temporal incoherence. Incident beams with some spatial incoherence but no temporal smoothing are compared to those with *ab initio* temporal beam smoothing (TBS). Under typical conditions, TBS beams will undergo far less angular and spectral spreading and far less SBFS than unsmoothed beams.

## 1 Introduction

The electromagnetic filamentation instability can occur whenever high intensity laser light interacts with long underdense plasmas. The instability is expected to occur in indirectly-driven inertial confinement fusion (ICF) hohlraums[1] and might also occur in the coronal interaction region of directly-driven ICF targets[2, 3]. It is a fundamentally important nonlinear laser-plasma interaction for two reasons. First, it has a relatively low excitation threshold, and can produce locally large intensity increases in a sufficiently long plasma. Second, as filamentation increases the local laser intensity, instabilities such as stimulated Raman (SRS) and Brillouin (SBS) scattering[4, 5, 6, 7], which otherwise might have been quiescent, can become readily accessible. Aside from altering the spatial and temporal distribution of the light intensity, filamentation also produces density and velocity striations in the plasma. These changes in the plasma environment can further change the behavior of nonlinear coherent processes such as SRS and SBS. The physics of these scattering instabilities is thus incomplete without a proper treatment of filamentation.

Much of the early work in this field centered around the properties of filamentation in its steady-state or stationary equilibrium limit[8]. Later, and with the application of large and fast computers to this problem, increasingly more complex models of both the plasma evolution [9] and laser light propagation [10, 11] were undertaken. These range from particle-in-cell codes that utilize electromagnetic wave descriptions coupled with Lorentz force particle pushers [5] (which are limited to rather small length and time scales) to more macroscopic descriptions using ray-tracing or parabolic (paraxial) wave equations for the light propagation

---

\*andrew.schmitt@nrl.navy.mil

with fluid-hydrodynamic plasma models [12, 13]. The code presented here falls in the latter category. It has been developed by merging an earlier version of a filamentation code[11], with an improved plasma hydrodynamic description[14] to include both full axial coupling and nonlinear plasma evolution in 2D. We call this new code PONHF2D (Paraxial Optics/Nonlinear Hydrodynamics for Filamentation in 2D). We use it to examine the qualitative and quantitative time-dependent behavior of filamentation and its companion instability, stimulated Brillouin forward scattering (SBFS), in plasmas.

Although the capability has existed for some time to treat large-scale time dependence of filamentation in plasmas, it is only recently that the hydrodynamics models used have included enough of the physics (e.g., complete axial coupling and the capability to address nonlinear ion waves and the proper inclusion of other instabilities such as SBFS) to properly answer many of the questions posed by filamentation. Of particular interest in this study is the effect of axial coupling in the plasma, which allows the light field at one axial position to affect the light field at other axial positions through a hydrodynamic, slow time-scale conduit. This interest is prompted in part by earlier studies that found qualitative differences in the behavior of light due to such hydrodynamic coupling[15, 16, 3].

The results presented here imply that the steady state limit of filamentation is seldom reached in realistic laser-plasma interactions. Our simulations show that the transient behavior of filamentation persists even for times large compared with characteristic hydrodynamic time scales. We also identify an *intrinsic* time dependent feature, the generation of spatial and temporal incoherence in the interacting light, that may make filamentation a useful feature of nonlinear light-plasma interactions. The simulations show that filamentation induces both a bandwidth in the transmitted light and scintillating striations in the plasma. The induced bandwidth and plasma striations can be large enough to eliminate further increases in filamentation and may hinder the growth of other instabilities[17], in a manner similar to external temporal beam smoothing (TBS) methods such as ISI[18] (Induced Spatial Incoherence) or SSD[19] (Smoothing by Spectral Dispersion). We find that the time dependence and smoothing of laser nonuniformities is a persistent feature of the filamentation interaction for times long compared to other characteristic laser-plasma interaction time scales.

## 2 Description of the code

In PONHF2D, laser propagation is modeled using the scalar parabolic (paraxial) wave equation:[11]:

$$2ik_0 \frac{\partial \Psi}{\partial z} = \left( \nabla_{\perp}^2 + \frac{\omega_0^2}{c^2} (\varepsilon(\mathbf{x}, t) - \langle \varepsilon(z, t) \rangle) - i \frac{\partial k_0}{\partial z} \right) \Psi \quad (1)$$

where  $\Psi$  is the slowly varying envelope of the em wave field assumed to be linearly polarized out of the plane of the simulation:

$$E(x, z, t) = \frac{1}{2} \Psi(x, z, t) e^{-i \int_0^z dz' k_0(z', t) + i \omega t} + c.c.$$

$k_0(z, t) = \omega \sqrt{\varepsilon(z, t)}/c$  is the wavenumber of the laser light in the plasma and

$$\varepsilon(\mathbf{x}, t) = 1 - \frac{\omega_p^2(\mathbf{x}, t)}{\omega_0^2} - i \frac{\omega_p^2(\mathbf{x}, t) \nu(\mathbf{x}, t)}{\omega_0^3}$$

is the dielectric constant in the plasma. The “ $\langle \dots \rangle$ ” notation applied to the dielectric constant in Eq. (1) is a spatial average in the direction transverse to the laser propagation, and  $\langle \varepsilon \rangle$  denotes the transverse-averaged dielectric constant. This equation describes the propagation of the laser light as a competition between diffraction [1st term RHS of Eq. (1)] and nonlinear refraction [2nd term RHS of Eq. (1)]; the 3rd term on the RHS of Eq. (1) corresponds to field swelling effects, and is negligible in plasmas that are approximately homogeneous. When nonlinear refraction is large enough to exceed diffraction (i.e., the filamentation threshold condition), the RHS of Eq. (1) is positive and the electric field intensity grows. Inverse bremsstrahlung absorption is included through the complex dielectric constant. Eq. (1) is solved for arbitrary incident laser fields using a fast-Fourier-transform (FFT) based split-step method[20].

The light propagation Eq. (1) is coupled to the plasma through the dielectric constant, which is primarily a function of the plasma density through the plasma frequency:  $\omega_p^2(\mathbf{x}, t) = 4\pi e^2 n_e(\mathbf{x}, t)/m_e$ . The electron density is found by solving the plasma fluid equations for the mass density.

Two different approaches are used to model the plasma response. The more general model uses a nonlinear two dimensional (2D) Flux-Corrected-Transport (FCT) algorithm[14] to solve the continuity equations for the plasma density and momentum, assuming a quasineutral one-fluid plasma. The equations solved in this case are:

$$\frac{\partial}{\partial t}\rho + \nabla \cdot \rho \mathbf{v} = 0 \quad (2)$$

$$\frac{\partial}{\partial t}\rho \mathbf{v} + \nabla \cdot \rho \mathbf{v} \mathbf{v} = -\nabla p - \alpha \rho \nabla E^* E - \rho \nu (\mathbf{v} - \mathbf{v}_0) \quad (3)$$

where  $\rho$  is the plasma mass density,  $\mathbf{v}$  is the plasma velocity,  $p$  is the plasma pressure,  $\alpha = Ze^2/2m_e m_i \omega_0^2$  is the coefficient of the ponderomotive force term,  $\nu$  is a heuristic damping coefficient (typically,  $\nu \sim 0.01 c_s/\lambda_0$  is used in the FCT simulations) and  $\mathbf{v}_0$  is the background spatially-averaged flow velocity. The plasma energy density is given by assuming an isothermal plasma, and ignoring local energy sources. The ideal gas equation of state closes the system of equations. The ionization level of the plasma and the plasma temperature are assumed to be known independently. This model ignores the effects of thermal filamentation and nonuniform inverse bremsstrahlung heating, as well as the PdV energy that goes into producing ion acoustic waves. Boundary conditions for the FCT algorithm are either (a) fixed (Neumann, Dirichlet, or mixed); (b) periodic; or (c) absorbing.

The second plasma model uses a spectral FFT based algorithm to solve the ponderomotively driven ion-acoustic wave equation. In Fourier space, the equations of continuity and momentum combine to produce:

$$\left( \frac{\partial^2}{\partial t^2} + qk \frac{\partial}{\partial t} + k^2 \right) \ln(n_e) = \left( \frac{\alpha}{2c_s} \right) k^2 E^* E. \quad (4)$$

$c_s^2 = (Z+1)T_e/m_i$  is the plasma acoustic speed,  $q=\nu/c_s k$  is the ratio of the acoustic wave damping to the acoustic wave frequency, and both  $\ln(n_e)$  and  $E^* E$  terms have been implicitly multiplied by the factor  $e^{i\mathbf{k} \cdot \mathbf{v} t}$  to account for a uniform background velocity flow. The time and space variables have been normalized by the quantities  $\lambda_0/c_s$  and  $\lambda_0$ , respectively. Eq. (4) is solved explicitly and exactly for constant or linearly time varying intensities using Laplace transforms. Although this spectral model is restricted to small amplitude density perturbations in a uniformly-flowing background plasma, it uses a more realistic damping model (it treats Landau damping of the ion-acoustic waves with the proper wavenumber dependence) and the implicit nature of the solution allows excellent retention of both amplitude and phase information. The model is similar to the previous model[11] except that it includes axial derivatives and a uniform background flow. This algorithm is used to verify the accuracy of FCT algorithm in linear regimes, it provides a measure of the sensitivity of the results to the particular damping model, and due to its accuracy and relative speed it is the preferred method when the driven density changes are linear. (The damping rate  $q=0.1$  is used in the spectral simulations except where noted.)

In summary, this version of PONHF2D improves upon its immediate predecessors in at least two ways. First, the hydrodynamics models now include background flow and can (with FCT) treat nonlinear plasma behavior. These features enable simulations in a wider range of realistic plasma conditions. Second, the plasma is axially coupled: the derivatives of the fluid variables in the direction of the light propagation are not ignored. This hydrodynamic axial coupling correctly describes both laser-plasma and plasma-plasma coupling in the time evolution of filamentation. With the addition of these features, this work complements recent studies on the effects of sheared transverse flow on filamentation [21, 22]. Preimposed stationary transverse flow was shown to deflect the beams towards the direction of flow by 5 or 6 degrees, typically. Without TBS we find that the angular spread of RPP beams in the absence of transverse flow is typically larger than 20 degrees. TBS leads to similar spreading of beams only at significantly higher intensities and for much longer plasmas.

### 3 Results

#### 3.1 Typical filamentation behavior

A canonical example of the filamentation behavior observed with PONHF2D is shown in Fig. 1. A laser with average intensity of  $1.8 \times 10^{15} \text{ W/cm}^2$  and  $0.35 \mu\text{m}$  wavelength is incident on a fully ionized, homogeneous He-H plasma with 2 keV temperature and  $0.1 n_{crit}$  density. The incident laser temporal profile rises linearly from zero to full intensity in  $125 \lambda_0 / c_s$  (100 psec), and is constant (and with no TBS) during the rest of the simulation ( $1250 \lambda_0 / c_s$ , or 1 nsec). The incident laser spatial profile is composed of 50 discrete plane waves, each at a different angle and with a randomly chosen amplitude and phase[11]; this models a generic laser beam with impressed spatial incoherence, and is similar on average to that given by an instantaneous ISI distribution, or generated with Random Phase Plate (RPP)[23] or Kineform Phase Plate (KPP)[24] optics. This beam is focused into the plasma with f/10 optics. Relatively little light is absorbed in this low density plasma (6.7%). This particular simulation uses the spectral hydrodynamics model, and the density changes produced by the light were  $< \pm 10\%$  peak-to-valley. This may be considered to be marginally in the linear regime; however a simulation with the same parameters but using the FCT method and  $\nu_{FCT} = 10^{-3}$  gives qualitatively and quantitatively similar results [the only exception being a slower transition to steady state (where it exists) due to the smaller ion wave damping].

The simulations show filamentation behavior that is qualitatively different than canonical steady state behavior. Three axially-separated regions are identified in which different behavior is found. In the first region, filaments rapidly form and focus, but then change little in time. In the second, a transition region, filaments begin to move side to side, oscillating in time, and are strongly deflected. In the third region, the filaments continue to change in time and angle, but deflections and time changes are more incremental and less violent than in the transition region. These three regions are described in more detail next.

In region I, encountered as the light begins its propagation into the plasma, there is a rapid filamentation and focusing down of the incident light. Many filaments form their first few foci in this region. After a short period of time, filamentation behavior in region I is qualitatively and quantitatively the same as that seen in a steady state simulation (Fig. 2b). The change from initial to stationary filamented intensity distributions occurs in times on the order of a few  $\lambda_\perp / c_s$ , where  $\lambda_\perp$  is the characteristic transverse size of the beamlet. In Fig. 1b, this steady-state-like region can be seen at time 312.5 (250psec) in the axial region  $0 < z < 600$  and in the center of the figure. At the sides of the figure, where the local average intensity is somewhat lower than average ( $50\% \langle I \rangle$ ) due to the particular realization of beamlets, the region extends further to almost  $1000 \lambda_0$ . Filamentation foci can be seen at a range of points including those at  $(x, z) = (290, 250)$ ,  $(180, 460)$  and  $(450, 700)$ .

This region should be consistent with steady state analytical theory [8, 11], in which filamentation growth is determined by a dimensionless parameter we refer to as the interaction strength [25]:  $\kappa_{pF} \equiv (n_e / n_{crit}) (\alpha / 2 c_s) = .009 (n_e / n_{crit}) \lambda_{\mu m}^2 I_{14} / (\sqrt{\epsilon} (1 + 1/Z) T_{e-keV})$ , where  $Z$  is the charge state of the ions,  $T_{e-keV}$  the electron temperature,  $I_{14}$  the local laser intensity in units of  $10^{14} \text{ W/cm}^2$ , and  $\lambda_{\mu m}$  is the laser wavelength in microns. Then, the fastest growing mode has the transverse wavenumber

$$k_{\perp - \text{fastest-growth}} / k_0 \simeq \kappa_{pF}^{1/2} \quad (5)$$

and the e-fold growth length

$$L_{\parallel - \text{growth}} = k_0 / (2\pi k_{\parallel}) \simeq \kappa_{pF} / (4\pi \epsilon^{1/2}).$$

In Fig. 1,  $\kappa_{pF} = 6.5 \times 10^{-4}$ , and the fastest growing hotspot should have a growth length of about  $420 (\langle I \rangle / I) \lambda_0$  and a transverse wavelength of about  $40 (\langle I \rangle / I)^{1/2} \lambda_0$ . The incident intensity distribution has a range of intensities up to about  $6 \langle I \rangle$ , so we expect the resulting distribution to have a corresponding range of growth lengths ( $L_{\parallel - \text{growth}} \geq 70 \lambda_0$ ) and strong unstable modes ( $\lambda_{\perp - \text{fastest-growth}} \geq 6 \lambda_0$ ). The filamentation structure in the stationary region I is in accord with these estimates.

Immediately after the light propagates through the first set of stationary filamented foci in region I, it enters a transition region (region II). Here, some of the filaments deflect at relatively large angles, in both directions [cf. Fig. 1c, at point  $(x, z) = (285, 640)$ , or Fig. 1(f) at  $(x, z) = (275, 1000)$ ]. This is similar to the

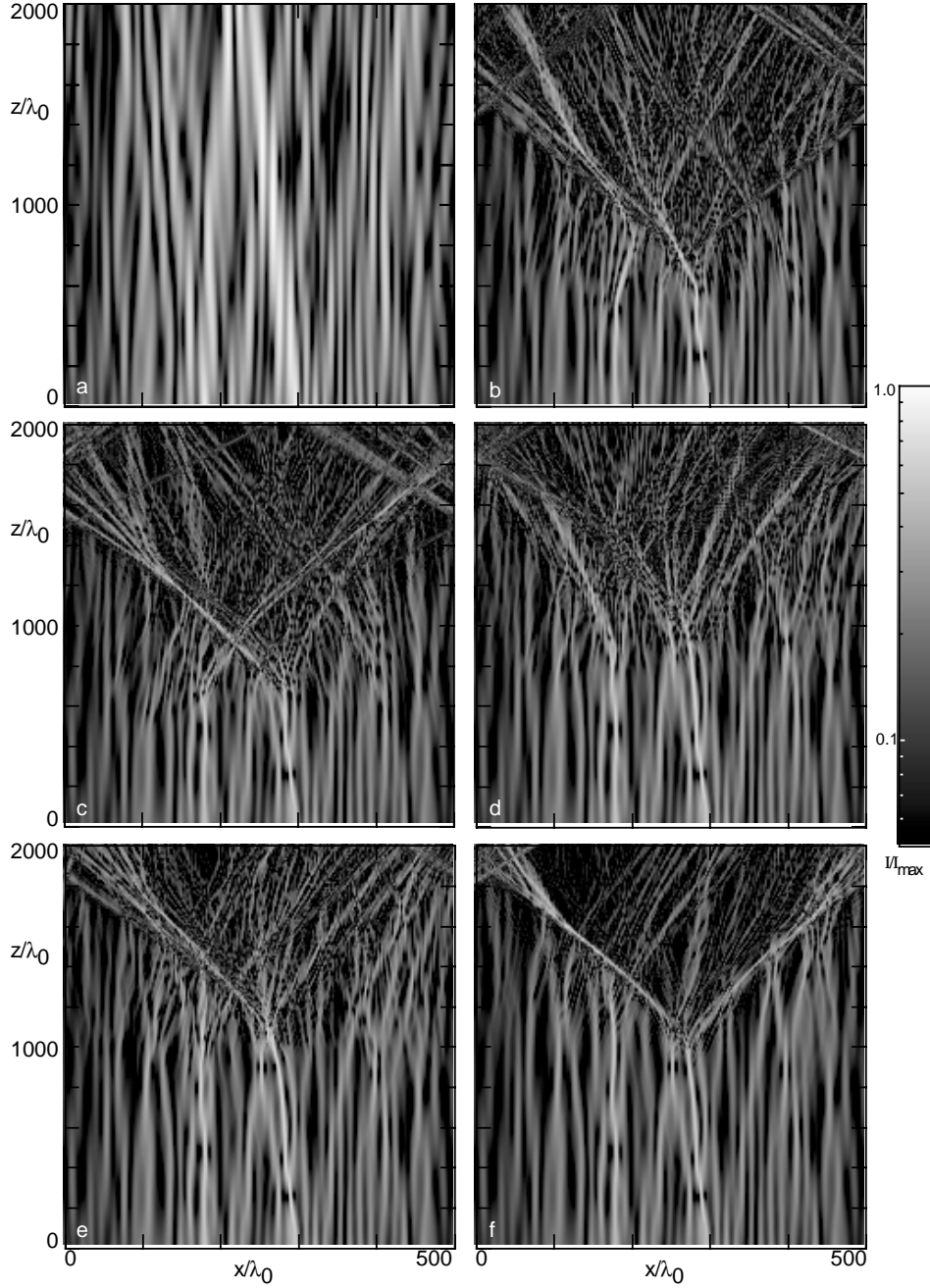


Figure 1: The instantaneous spatial distribution of the intensity in the plasma at six different times during the filamentation simulation, (a)  $t=0$ ; (b)  $t=312.5$ ; (c)  $t=375$ ; (d)  $t=625$ ; (e)  $t=937.5$ ; (f)  $t=1250$ . [Times are in units of  $\lambda_0/c_s$  (0.8 psec)]. Laser light with  $0.35 \mu\text{m}$  wavelength,  $2 \times 10^{15} \text{W/cm}^2$  intensity and  $f/10$  optics is incident from the bottom of the box. The plasma is He-H at  $0.1n_{crit}$  and 2 keV. The active area of the simulation is  $2000\lambda_0$  ( $700 \mu\text{m}$ ) long by  $500\lambda_0$  ( $162.5 \mu\text{m}$ ) wide, and there is an additional  $500\lambda_0$  buffer region of plasma before and after the light propagation region ( $-500\lambda_0 < z < 0$  and  $2000\lambda_0 < z < 2500\lambda_0$ ) where no interaction occurs. There is no bandwidth in the incident beam aside from that imposed by the laser time profile, which is linearly ramped from  $t=0$  to  $t=100$  psec, after which it is held constant. (The scale in each image is independently normalized to the maximum intensity at that time.)

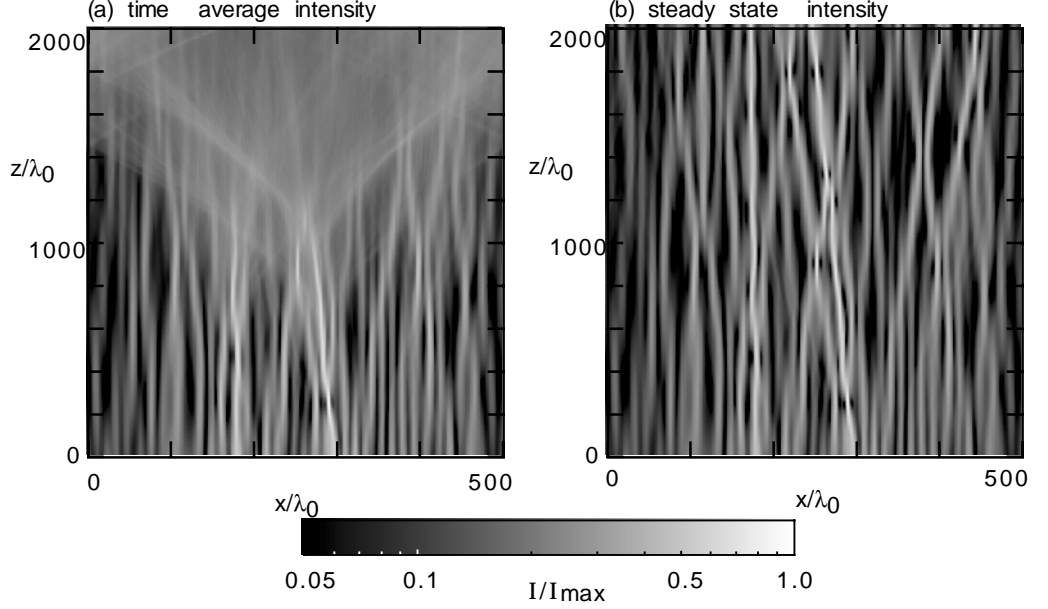


Figure 2: (a) The time averaged spatial intensity distribution for the simulation shown in Fig. 1 and (b) the time asymptotic ( $t = \infty$ ) intensity distribution from a steady state simulation with the same parameters as (a).

break up and spreading of beamlets into many filaments that has been seen in earlier simulations[26, 11], but here the spreading and breaking up is an inherently dynamical process. The dynamic deflections make many of the filaments appear to “dance” as time goes on, turning with positive and negative angles with respect to the propagation direction. A close-up of this behavior for a particular beamlet is shown in a sequence of pictures in Fig. 3. These sequences show a filament bending both left and right and breaking up to smaller filaments at the same time. Beamlets or filaments first steepen axially and finally spray out in angle and continue to break up into smaller filaments. They accelerate sideways according (roughly) to the size of the axial curvature they achieve just prior to the breakup of the filament [27, 15]. Filaments can readily overtake and cross over each other in their sideways motion as they fan out and foliate. This dynamically multifoliating picture gives the impression of a set of dancing beamlets fanning out both ways from the strongest filaments to cover the whole beam. As the filaments bifurcate and lose strength, their sideways acceleration is diminished, newer beamlets come to fill in the same space, and the process continues for a great many ion acoustic time periods.

Details of the transition to nonstationary behavior in region II can be seen in Figs. 4 and 5. Here we show the angular distribution of the light vs. propagation distance at a single time ( $375\lambda_0/c_s$ , or 300 psec; cf. Fig. 1c). A rapid increase in angular divergence occurs where the filaments first show a large deflection (about  $z=650\lambda_0$ ). The angular width of the beam almost doubles in the distance of about  $150\lambda_0$  around this point (cf. Figs. 4d and 4e). The bandwidth of the light exhibits a similar broadening at this point as well (Fig. 5).

In order to delineate the start of region II we follow a characteristic local variable of the interaction as a function of propagation distance and time. As an example, consider the transverse-maximum intensity displayed in Fig. 6a. A boundary is clearly seen between the end of region I (the lower right hand section of the figure, where the intensity is time independent) and the beginning of region II (the time-dependent region in the upper half of the figure, where the intensity maxima are continually changing). The position of this boundary moves rapidly into the plasma at first (until time  $\approx 200$ , or 160 psec), and then continues

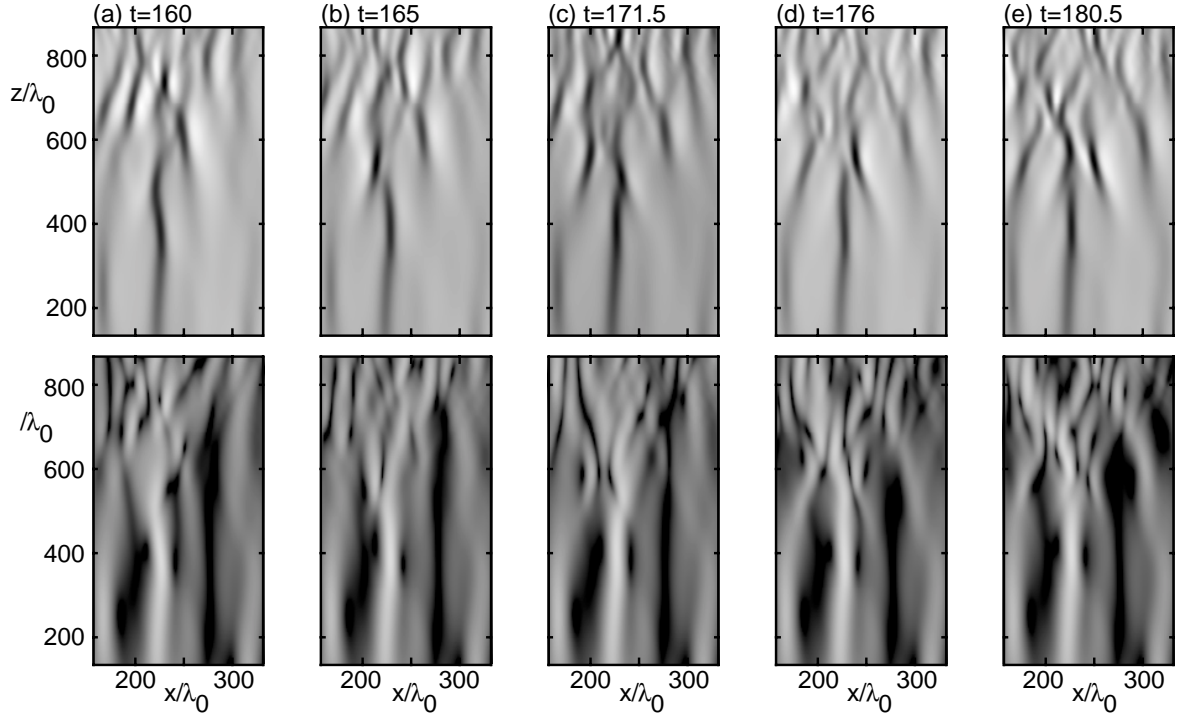


Figure 3: A sequence of density (top) and the corresponding laser intensity (bottom) spatial distributions for a subset of the simulation, at successive times shows the movement of a filament in the transition region II giving rise to bifurcations and fanning out of the intensity distribution. The times shown are (a)  $t=160$ ; (b)  $t=165$ ; (c)  $t=171.5$ ; (d)  $t=176$ ; (e)  $t=180.5$ . In the upper images, dark areas correspond to values below average density, bright areas are regions above average. The scale for the intensity images on the bottom is as in Fig. 1.

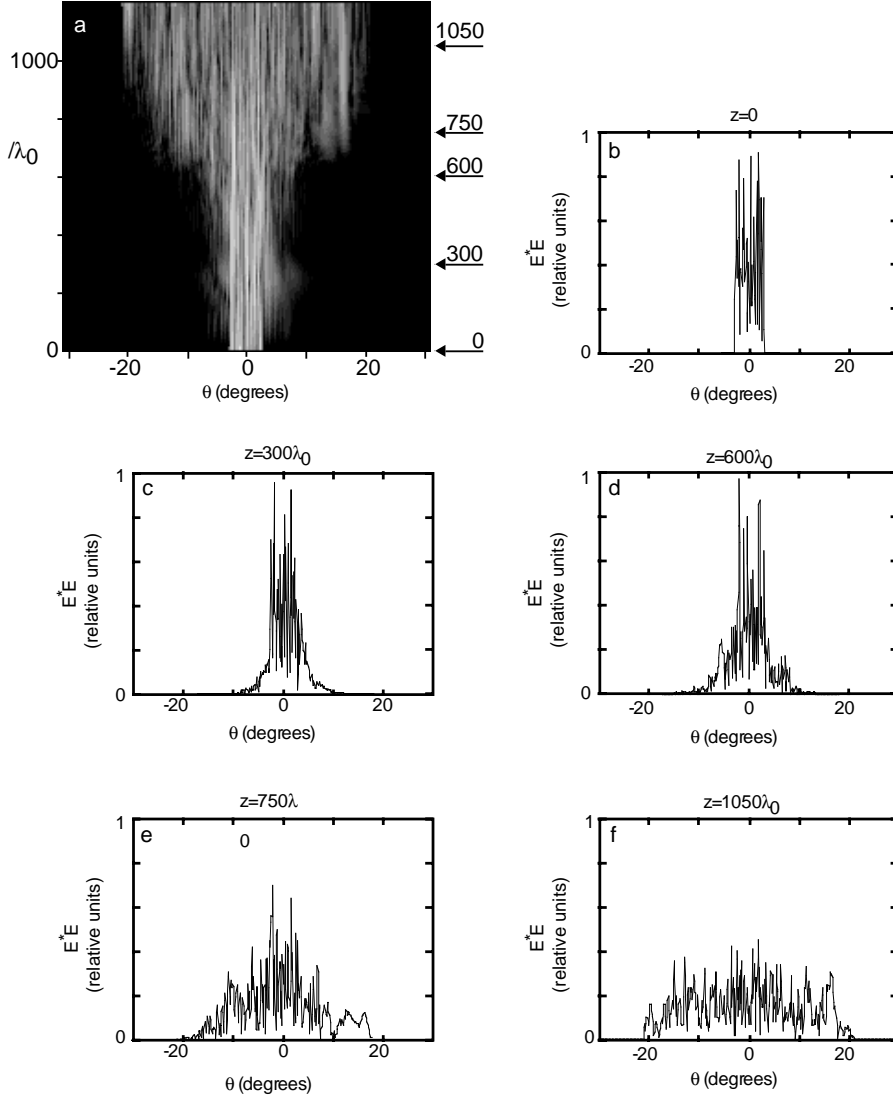


Figure 4: The angular distribution of the light in the plasma at consecutively larger propagation distances at  $t=375 \lambda_0/c_s$  (300 psec) for the simulation in Figs. 1c. The image in the upper left hand side of the figure is the intensity distribution as a function of angle and propagation distance; the other five plots show line-outs of this image at the positions noted by the small arrows to the right of the image. As the light propagates through the transition region  $z \approx 650\lambda_0$ , the bandwidth of the beam rapidly increases and the central unshifted frequency component shrinks and disappears into the rest of the spectrum.



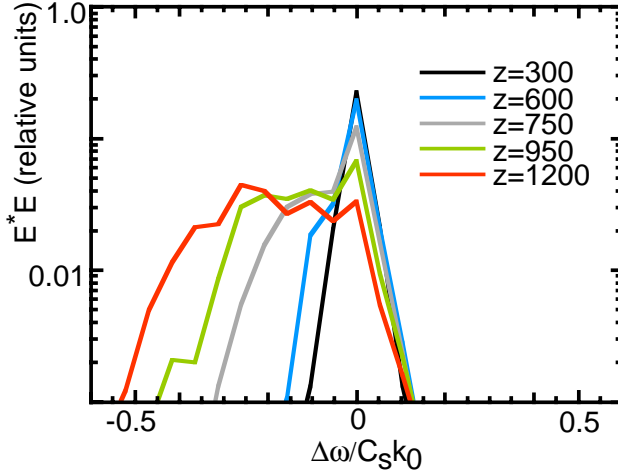


Figure 5: The spectra of the light in the plasma at consecutively greater propagation distances show that the bandwidth rapidly increases at the same point ( $z \approx 650\lambda_0$ ) that the angular width broadens. These spectra are taken at the same simulation and time as shown in Fig. 4.

further in at a much slower rate. The movement of region II slows as the interaction strength is increased (Fig. 6b), and sometimes halts for long periods of time in the most intense interactions. Although the specifics of any particular realization are sensitive to both plasma (e.g., density, temperature, damping) and laser characteristics (e.g., intensity,  $f/\#$ , bandwidth), these qualitative features hold true in general. In all cases, the time for the plasma to equilibrate can be considerably longer than local hydrodynamic times [i.e., acoustic transit times across local beam structures (speckles) or simulation dimensions].

Region III begins just after the first large-angle deflections of filaments in region II have swept by a large portion of the beam. This final region is marked by the many interactions, crossings, and rapid motion of multiply bifurcated filaments. [As an example, we consider the region ( $x \approx 300$ ,  $z > 1200$ ) in Fig. 1d to be in region III.] The dancing motion of the filamentary structures in region III, triggered by the multifoliation behavior in region II, is typically faster than the local plasma acoustic speed, and the plasma is unable to fully respond to them. Thus, peak to valley local density variations are not as pronounced as in regions I or II. From the point of view of a filament, the deflections it undergoes are no longer caused by the density striations it or a nearest neighbor have dug, but those which result from the interaction of many filaments with the plasma over an extended time period. As a result, the density and intensity fluctuations become decorrelated (Fig. 7) and the intensity distribution, averaged over time, becomes much smoother (cf. Fig. 2a). Fig. 8 compares the incident intensity profile to a typical transmitted one and its time-average over the entire simulation. The peak-to-valley time-averaged intensity (Fig. 8d) decreases with time at least as fast as  $t^{-1/2}$  (which is the typical rate of TBS schemes).

Another way to characterize the induced beam smoothing is by imaging the transmitted light as a function of transverse position and time as shown in Fig. 9. The transmitted intensity structure shows that both temporal and spatial incoherence is continually impressed on the light via its interaction with the plasma. At early times ( $t < 100$  or 80 psec), the intensity is low, filamentation has not yet begun, and the transmitted intensity changes slowly in time. As the laser intensity rises through the filamentation threshold, the transmitted intensity begins changing rapidly in time and space. Little repeatable or predictable structure is seen, and both the time and spatial scales of the intensity variations are much smaller than those present in the incident beamlets, indicating induced spatial and temporal incoherence. This incoherent behavior associated with region III continues unabated to the end of the simulation.

The results presented so far, which we believe to be representative of time-dependent filamentation and SBFS behavior, show that filamentation does not approach steady state monotonically or uniformly.

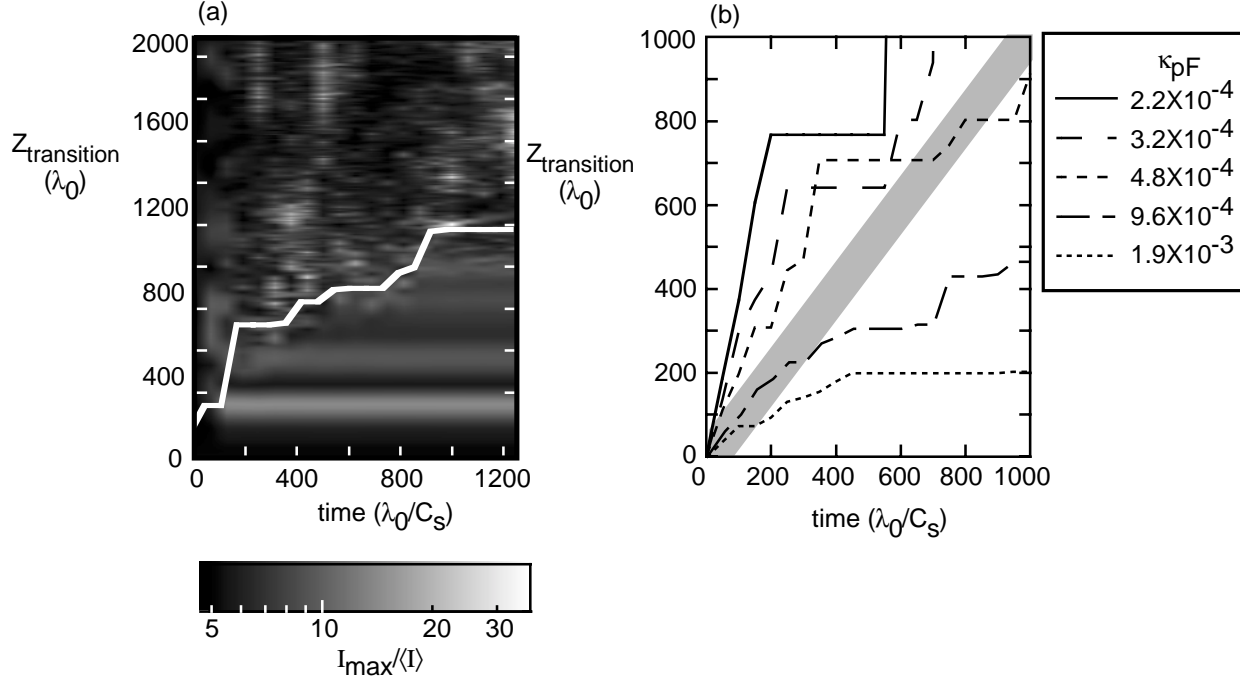


Figure 6: (a) Image of  $I_{max}$ , the maximum intensity, as a function of propagation distance and time; also shown is the boundary separating the time-independent and time-varying regions. The boundary point is defined by the requirement that the local  $I_{max}$  equilibrates to within 10% of its final value in time. The movement of this point follows the transition region mentioned in the text. The results shown in (a) are from the simulation shown in Fig. 1. (b) Equilibrium trajectories for a series of runs in which only the interaction constant was varied. The thick gray line on the plot extending from  $\{t,x\} = \{0,0\}$  to  $\{1000,1000\}$  is the trajectory of a hypothetical ion-acoustic wave launched into the plasma at  $\{0,0\}$ , and indicates the longest characteristic hydrodynamic time of the system.

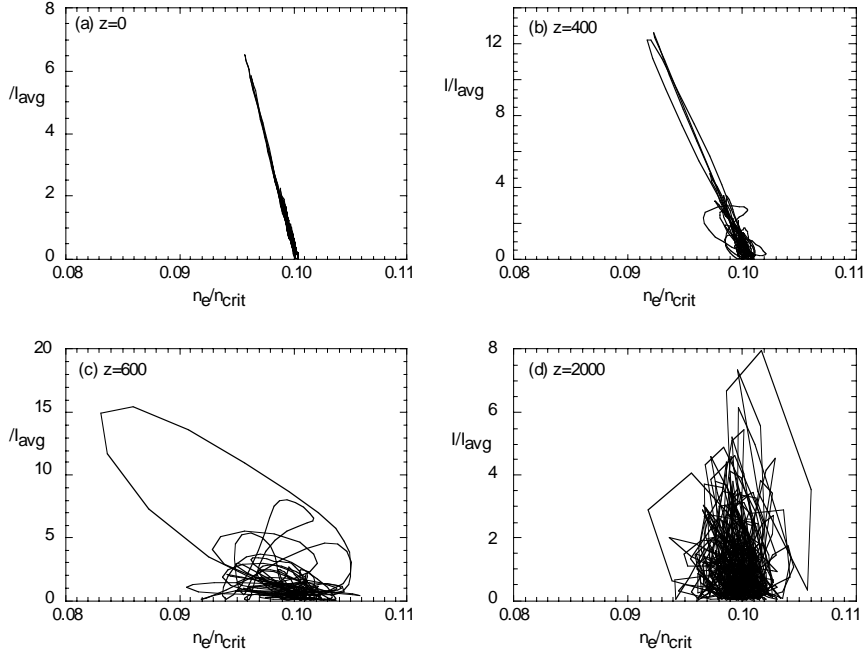


Figure 7: The correlation plots between the intensity and density in the plasma at different propagation distances into the plasma show that the intensity and density in region I are highly correlated (a), they lose correlation (b) as the interaction transitions to region II (c) and are uncorrelated in region III (d). These plots are from the same simulation and time as shown in Fig. 4.

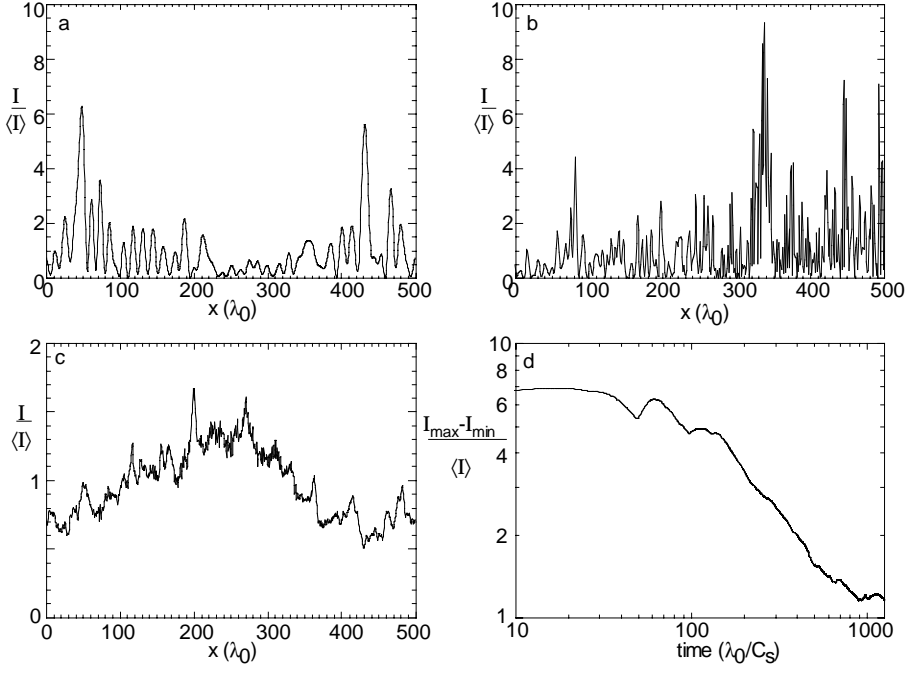


Figure 8: The light intensity in the plasma shows evidence of smoothing during the simulation. Compare the intensity at (a)  $z=0$  and (b)  $z=2000\lambda_0$  at time  $625\lambda_0/c_s$ , and (c) the intensity at  $z=2000\lambda_0$  time averaged over  $1250\lambda_0/c_s$ . (d) The time-averaged peak-to-valley intensity as a function of time. The intensity range only begins to show the effects of smoothing once the laser is near full power ( $t=125$ ). All data is from the simulation in Fig. 1

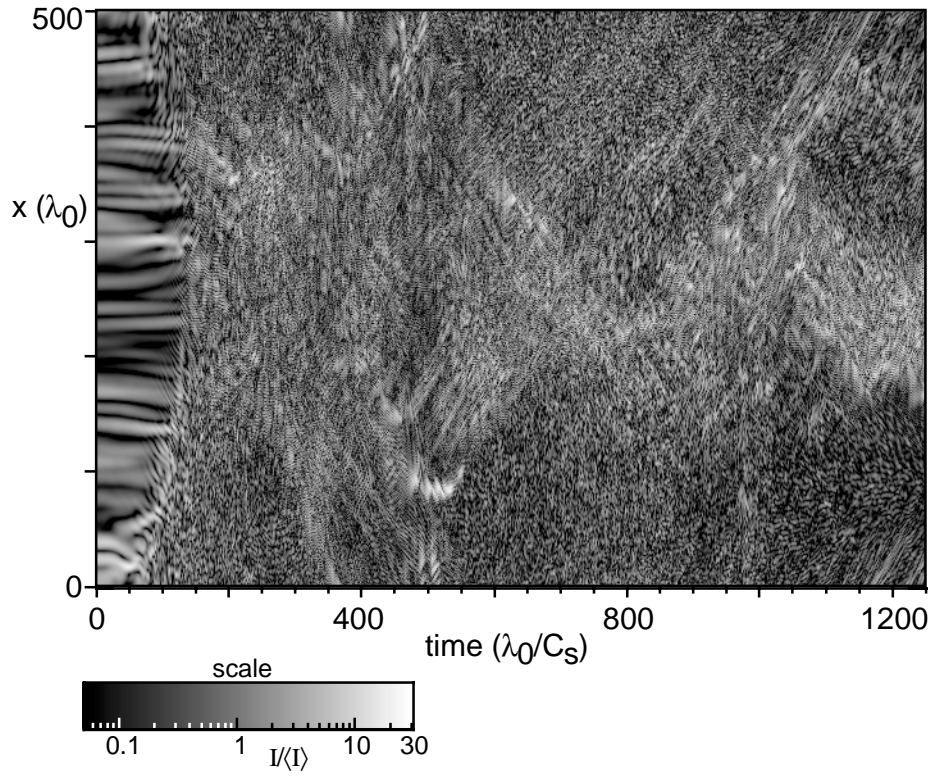


Figure 9: The transmitted intensity through the plasma as a function of transverse spatial dimension and time (i.e., shown as if a streak camera were measuring the output intensity), for the simulation shown in Fig. 1.

Much of the plasma is not even approximately in equilibrium during the simulation (i.e.,  $z > 1000\lambda_0$ ). Generally, equilibration is quick in the initial region I, which includes the first (few) foci. In the following transition region II, the filaments begin to dynamically multifoliate and strongly deflect left and right. The resulting acoustic waves induce or increase the deflection of weaker filaments, accumulatively giving rise to dancing beamlets. Hence the beamlets are seen to spray outward and continuously dance about, producing intensity distributions that approach optically smoothed distributions. In this final region, the light becomes successively more decorrelated with the plasma response and increases its spatial and temporal incoherence. Equilibration occurs quickly in region I, and then much more slowly in regions that are initially in region II or III. Equilibration in these latter regions only occurs when the region I/II boundary passes through them.

### 3.2 Variation of filamentation with interaction strength

Evidence of induced incoherence in the propagating light is seen in many of the previous results: filaments passing through region II show angular broadening and bandwidth enhancement (Figs. 4 and 5); time-averaged intensity variations decrease in time at a rate similar to and even exceeding  $t^{-1/2}$  (Fig. 8), resulting in smoothed light distributions (Fig. 2); and higher frequency variations in both spatial and temporal scales are seen in the transmitted light (Fig. 9).

Systematic evidence for the inducement of temporal incoherence is found by analyzing the spectra of the transmitted light as the interaction strength is varied (Fig. 10). (This series of runs simulates a generic f/10 0.25 micron laser incident on a homogeneous nonabsorbing box of CH plasma at  $0.5n_{crit}$  and 1 keV, 500 wavelengths wide by 2000 long. Only the middle  $1000\lambda_0$  section of the plasma interacts with the laser. The interaction strength was changed by varying the intensity from  $7 \times 10^{13}$  to  $6 \times 10^{14} \text{ W/cm}^2$ ) The spectra shows that the light has undergone both a frequency broadening and a shift towards lower frequency (red-shift). More precisely, since not all of the light is scattered (note the usually strong fundamental in the spectra), there is a broad spectrum superimposed on the original. The spatial incoherence shows a similar broadening as the interaction strength increases (Fig. 11). In contrast to the bandwidth, the increased angular spread is symmetric about the forward direction. Also note that the variation with  $\kappa_{pF}$  looks quite similar to the variation with propagation length seen in Fig. 4.

In general both the spectrum and angular distributions increase in breadth, and the spectrum increasingly red-shifts, as the interaction strength of the coupling increases. Fig. 12 summarizes the results of Figs. 10 and 11. At higher intensities, the spectral width approaches  $c_s/\lambda_0 \sim 1 \text{ psec}^{-1}$ , which is a typical *incident* bandwidth for a TBS laser beam. Thus, the bandwidth associated with filamentation can produce the same effects as TBS; the drawback is that the laser beam must first suffer filamentation, the associated intensity increases, and the risks of other induced instabilities.

While the bandwidth of the transmitted beam can be similar to an incident beam with TBS, the angular distribution is typically much broader (Fig. 12c). The incoming beam (in this case f/10) changes to a much broader angular range (as much as f/1.3). This large angular divergence would make it more difficult to focus or spatially localize such a beam. The data also shows that there may be the beginning of a turn over in the angular width as a function of interaction strength. The paraxial wave description is of questionable validity at this point, as the light is spreading in the region  $\pm 22$  degrees. A different approach, preferably using a temporally enveloped but spatially unapproximated wave equation formulation for the laser light, is needed to address this behavior definitively (this modification is planned for the next version of PONHF2D).

The angular broadening seen in the laser light is larger than what would be expected on the basis of ponderomotive filamentation alone. The expected broadening can be estimated as that angle produced by the fastest growing mode in the ponderomotive filamentation dispersion relation (eq. 5):

$$\theta_{max} \simeq k_{\perp - \text{fastest-growth}}/k_0 = \kappa_{pF}^{1/2}.$$

The predicted angular filamentation spread is much less than the observed spread (Fig. 12c) unless in situ maximum intensities are used to calculate the interaction strength (which then track the broadening only at the highest interaction strengths). In fact the large angles seen in the simulation are an inherent feature of the time dependent interaction, as can be seen by comparing Figs. 1 and Fig. 2

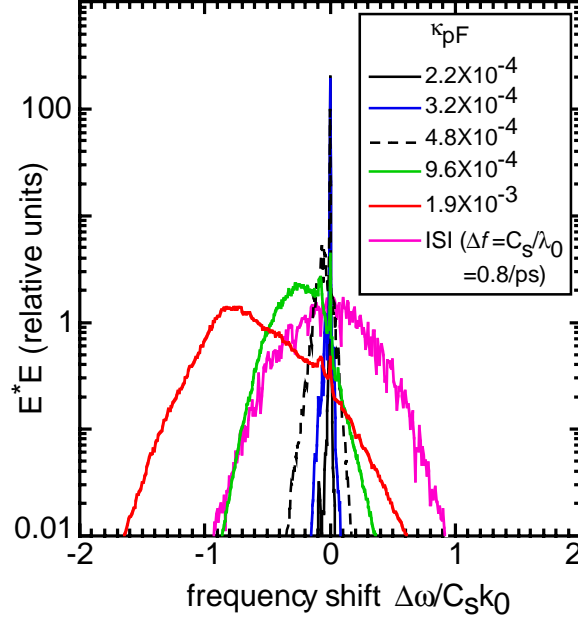


Figure 10: The spectrum of transmitted laser electric field, shown as a function of the frequency shift ( $\Delta\omega/c_s k_0$ ), widens as the interaction strength increases. All other parameters of the simulation were held constant. Also shown, for comparison, is a typical spectrum produced by ISI.

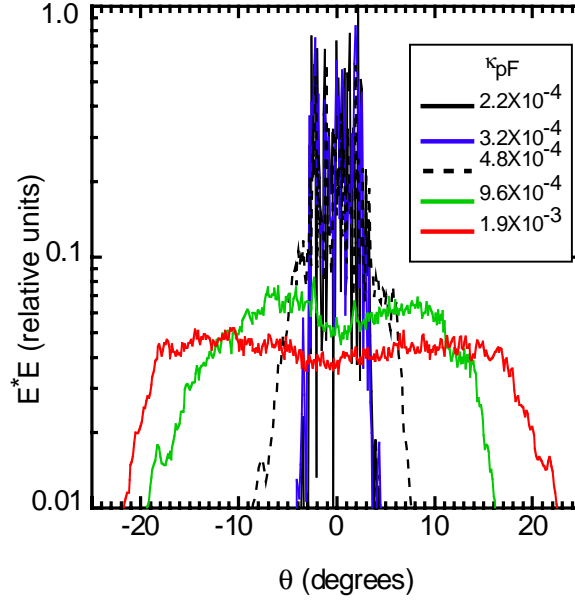


Figure 11: The transmitted laser electric field is shown as a function of the output angle, for five different interaction strengths. All other parameters of the simulation were held constant. The incident light distribution was restricted by the focusing optics to the angular range  $|\theta| < 2.9$  degrees.

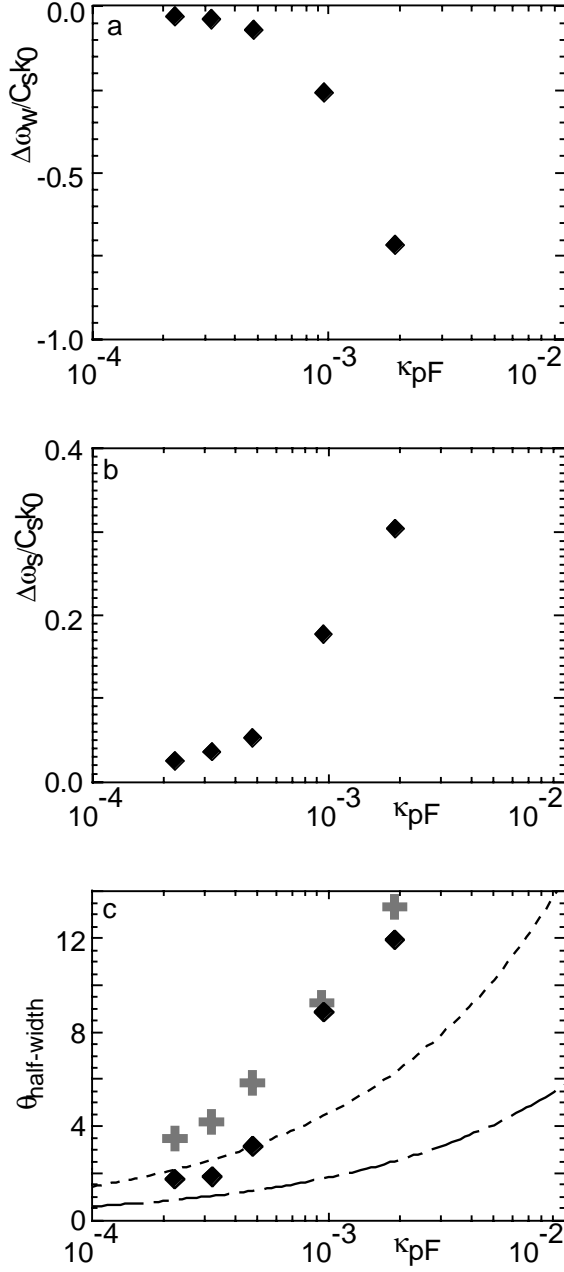


Figure 12: Variation of the transmitted (a) spectral width, (b) spectral shift, and (c) angular width as a function of interaction strength,  $\kappa_{pF}$ . The dash-dotted and dotted curves in (c) show the expected width using the fastest growing mode from steady-state filamentation theory, and using either the average intensity (dash-dotted) or the maximum incident intensity (dotted). The grey cross points in (c) show the expected width using the maximum intensities found in the plasma during the simulation.



An additional contributor to the angular broadening is the stimulated Brillouin forward scattering (SBFS) instability [28, 4]. In this scenario, as the filaments are formed and produce their expected (filamented) angular distribution, the enhanced angular distribution stimulates more SBFS (which grows more strongly with angle). The SBFS which starts from the finite-angle pump further widens the angular distribution of the transmitted light. This SBFS-enhanced wider angular distribution in turn can be a feedback to the filamentation, and cause filaments to propagate at larger angles, as in Fig. 1.

### 3.3 Stimulated Brillouin Forward Scatter

The diagnosis of SBFS is supported by the combined angular and spectral dependence of the transmitted light. Fig. 13 shows the transmitted intensity as a function of its frequency shift and angular direction. The locus of brightness in this image gives the dispersion relation for the scattered light. The frequency-broadened red shift seen earlier in Fig. 5 and Fig. 10 is due to averaging a narrowly-peaked spectra that shifts proportionately with angle. The frequency shift is approximately linear with the scattering angle for the range shown, consistent with SBFS. SBFS obeys the dispersion relation [28, 4]:

$$(\omega_s^2 - \omega_{pe}^2 - c^2 k_s^2) \left[ (\omega_0 - \omega_s)^2 - 2i(\omega_0 - \omega_s)\nu_{ia} - c_s^2 |\mathbf{k}_0 - \mathbf{k}_s|^2 \right] = 2\gamma_0^2 \omega_0^4, \quad (6)$$

where the coupling coefficient is given by

$$\gamma_0^2 = \frac{1}{8} \left( \frac{v_0^2}{c^2} \right) \left( \frac{|\mathbf{k}_0 - \mathbf{k}_s|^2}{k_0^2} \right) \left( \frac{\omega_{pi}^2}{\omega_0^2} \right). \quad (7)$$

Here  $\omega_0$  and  $\omega_s$  are the pump and Brillouin scattered light wave frequencies, and  $\omega_{pe}$  and  $\omega_{pi}$  are the electron and ion plasma frequencies. The ion wave damping rate is  $\nu_{ia}$ , and the light and sound speeds are  $c$  and  $c_s$ , respectively. This dispersion relation contains both the weak and strong ion wave damping limits as well as the weak and strong coupling limits. To write down the solution, it is convenient to use a scaled and shifted complex frequency variable,  $\delta$ , in terms of which the ion acoustic wave frequency is:

$$\omega_{ia} = (\omega_0 - \omega_s) = c_s k_{ia} + \delta \gamma_0^{2/3} \omega_0 = \gamma_0^{2/3} \omega_0 (\Omega + \delta) \quad (8)$$

where

$$\Omega = \frac{1}{\gamma_0^{2/3}} \frac{(c_s k_{ia})}{\omega_0}. \quad (9)$$

In terms of physical variables, and the expression for wavevector matching,  $k_{ia} = 2k_0 \sin(\theta_s/2)$ ,  $\Omega$  becomes:

$$\Omega = 0.606 \left( \frac{Z}{A} \right)^{1/6} \frac{T_{e-keV}^{1/2}}{[n/n_c I_{14} \lambda_{\mu m}^2]^{1/3}} [2 \sin(\theta_s/2)]^{1/3}, \quad (10)$$

where  $A$  is the ion mass number and  $\theta_s$  the SBS scattering angle with respect to the forward direction. For typical ICF laser plasma conditions,  $\Omega$  is of order one or less, implying that strong coupling effects are not ignorable. In terms of these variables and  $\nu_{LD} = \nu_{ia}/c_s k_{ia}$ , the dispersion relation for SBFS becomes the following cubic in  $\delta$ :

$$\delta [\delta^2 + 2\Omega(1 - i\nu_{LD})\delta - 2i\Omega^2\nu_{LD}] + 1 = 0. \quad (11)$$

In the weak coupling and negligible damping limit, ( $\Omega \gg 1, \nu_{LD} \ll 1$ ) the unstable root of eq. (11) approaches  $\delta^{WC,ND} \sim -i/\sqrt{2\Omega}$ . In the strong damping limit, ( $\nu_{LD} \gg \Omega^{-3/2}$ ), the unstable root is  $\delta^{SD} \sim -i/(2\Omega^2\nu_{LD})$ . Finally, in the strong coupling limit, ( $\Omega \ll 1$ ) the unstable root approaches  $\delta^{SC} \sim \exp[-2i\pi/3]$ . We can also give a general expression for the root of this cubic which bridges the gaps between these various limits:

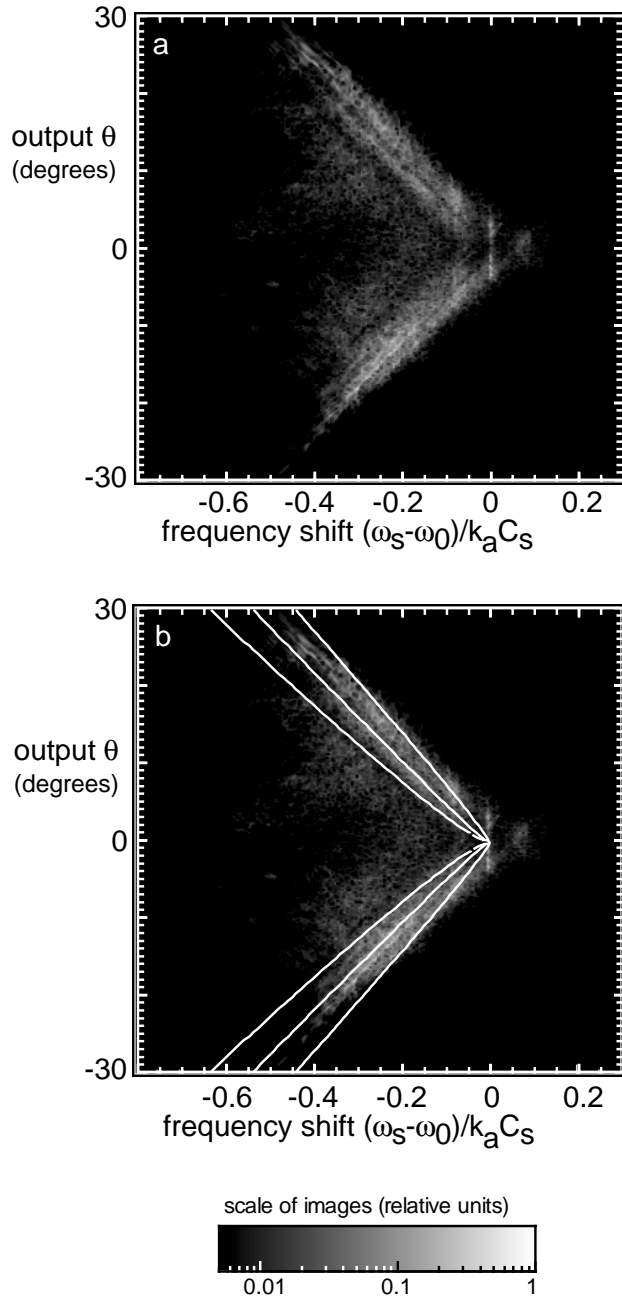


Figure 13: The transmitted spectrum of the laser electric field is shown as a function of frequency and scattering angle, for the simulation shown in Figs. 1. (a) contains just the simulation results, while (b) is the same but with the overlaid dispersion relation from SBFS theory: the red shift is given by the central line, while the left and right hand lines give the expected bandwidth from the growth rate.

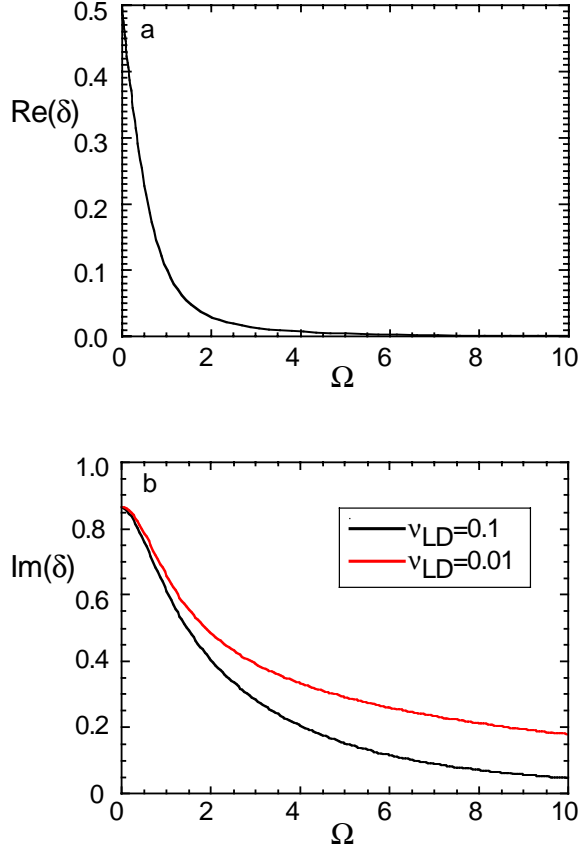


Figure 14: The (a) real and (b) imaginary parts of the general dispersion relation for SBFS given in the text, Eq. 12.  $\text{Re}(\delta)$  is proportional to the nonlinear frequency shift of the scattered light, while  $\text{Im}(\delta)$  is proportional to the growth rate for SBFS. In (b) the imaginary part for two different damping rates are given.

$$\delta^{SBS} = -\frac{2}{3}(1 - i\nu_{LD})\Omega + \frac{(2\Omega^2(1 - i\sqrt{3})(2\nu_{LD}^2 + i\nu_{LD} - 2))}{D^{1/3}} - \frac{1}{3 \times 2^{4/3}} \left( (1 - i\sqrt{3})D^{1/3} \right), \quad (12)$$

where

$$D = -27 - 16(1 - i\nu_{LD})^3\Omega^3 - 36i(1 - i\nu_{LD})\nu_{LD}\Omega^3 + 3^{4/3}\sqrt{D_2} \quad (13)$$

and

$$D_2 = 27 + 32(1 + i\nu_{LD}^3)\Omega^3 - 24(1 + i\nu_{LD})\Omega^3 + 16\nu_{LD}^2\Omega^6(1 - \nu_{LD}^2). \quad (14)$$

We have plotted in Fig. 14 the behavior of the real (frequency shift) and imaginary (growth rate) parts of  $\delta$  as a function of  $\Omega$ . In the case of the imaginary part of  $\delta$ , we have plotted it for two values of the Landau damping fraction  $\nu_{LD} = 0.01$  and  $\nu_{LD} = 0.1$ , which are characteristic weak and strong damping values, respectively. Note that for typical conditions in ICF laser-plasmas, the local laser intensity dependent frequency shift due to strong coupling is of the order of 10–20% of  $\omega_{ia}$ . This is consistent with the simulation data shown in Figs. 15(d),(e).

Using eq. 8, these can be converted to physical frequency shifts and growth rates. Fig. 13b directly compares this formula to the simulation presented in section III.A. At higher powers we observe *multiply scattered* SBFS, as the dispersion relation diagnostic shows by having multiple distinct streaks (15c-e).

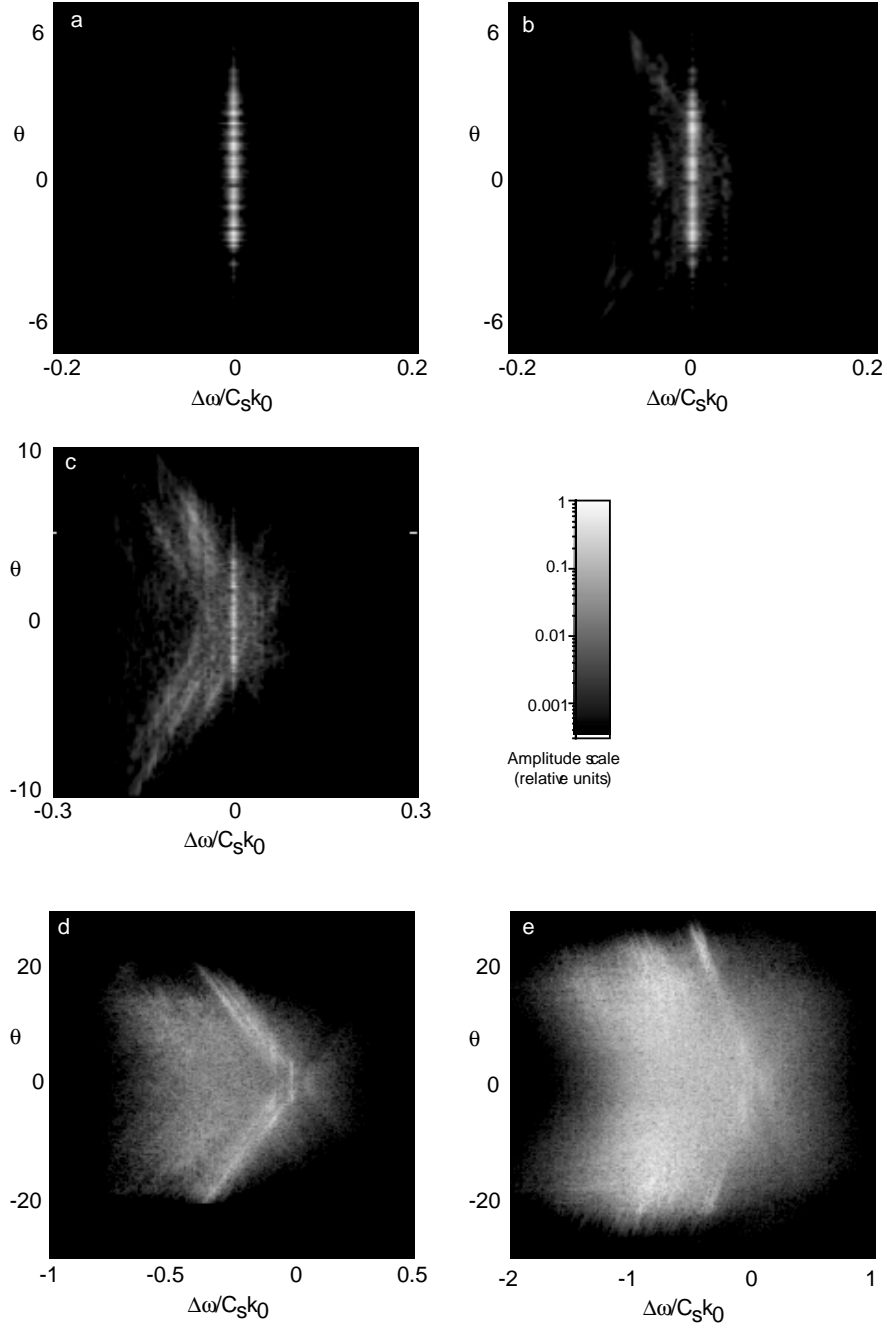


Figure 15: The output spectrum of the laser electric field as a function of frequency and scattering angle, for increasing interaction strength shows the spectrum broadening in both angle and frequency. (a)  $\kappa_{pF} = 2.2 \times 10^{-4}$ ; (b)  $\kappa_{pF} = 3.2 \times 10^{-4}$ ; (c)  $\kappa_{pF} = 4.8 \times 10^{-4}$ ; (d)  $\kappa_{pF} = 9.6 \times 10^{-4}$ ; (e)  $\kappa_{pF} = 1.9 \times 10^{-3}$ .

Clearly, multiple resonant scattering will spread the beam divergence considerably. A more realistic model for SBFS where the initial scattering levels are kept low due to frequency modulations of the ion waves via intensity variations [30] or flow nonuniformities [17] would severely limit multiple rescattering and thus diminish the observed angular spread.

The SBFS comes mostly from the transition region II, where the light is changing most strongly in time (cf. Fig. 5), and also from region III. In region II, the multifoliating behavior of the beamlets is consistent with SBFS in the way the light “bounces” off ion acoustic waves (IAWs) that it generates (cf. Fig. 3). As a beamlet bends to the right, it sheds an IAW to the left (with the proper SBFS scattering geometry). This bending to the right in turn produces an IAW that propagates to the right (in turn causing the light to turn back to the left). Additional SBFS is produced in region III, because the light there encounters enhanced (nonthermal) levels of ion acoustic waves generated by the plasma puncturing action of all the multifoliated filaments. (This anticorrelation between SBFS and coherent filamentation has been anticipated in previous work [29]).

### 3.4 Filamentation with incident optical smoothing

If time dependent filamentation and SBFS can induce bandwidth in incident monochromatic light, what will happen to light that already has bandwidth? We simulate ISI beams and increase the interaction strength until similar magnitude effects are observed. [Previous unpublished studies by one of the authors (AJS) have shown that filamentation is reduced or suppressed by ISI and (two-dimensional) SSD beams similarly when similar bandwidths are used]. As expected, a much larger interaction strength parameter is needed before any filamentation effects are seen, since TBS produces much smaller changes in the plasma density than an equivalent unsmoothed (RPP) beam. However, if we increase the interaction strength enough, the bandwidth of the TBS beam increases, with the red-shifted shape indicative of SBFS. Fig. 16 shows simulation results for TBS light with an incident bandwidth  $\Delta f = c_s/\lambda_0 \simeq (0.8 psec)^{-1}$ . The TBS beams are incident on the same plasma described in Fig. 1. For a similar intensity ( $2 \times 10^{15} W/cm^2$ ,  $or \kappa_{pF} = 7.2 \times 10^{-4}$ ), the light passes through the plasma virtually unchanged. Doubling and quadrupling the interaction strength produces increasingly strong red shifted peaks and a corresponding broadening in the transmitted spectra, similar to the unsmoothed incident beams. As the light broadens in frequency, it also broadens in angle. Again, as for unsmoothed beams, bandwidth is only gained with an increase in transmission angle. The angularly resolved spectra for the most intense interaction (Fig. 16c) shows a red-shifted feature in accordance with SBFS theory.

## 4 Conclusions

We have presented simulation results of time dependent ponderomotive filamentation using a parabolic (paraxial) scalar wave equation model for the laser and a flexible two dimensional hydrodynamic model for the plasma. We have shown that time dependent filamentation causes the filaments to take the form of “dancing beamlets” in plasmas and that this movement impresses both temporal and spatial incoherence on the laser beam propagating through a plasma. We identified three separate regions of behavior. Near the input plane, the filaments reach their first foci and come into a equilibrium with the plasma relatively quickly. This is followed by a transition region (II) where large deflection of the beamlets and further breakup into filamentary structures are seen including SBFS. This region is characterized by multifoliation, fanning and successively bifurcating filaments. These filaments deflect both left and right with respect to their initial propagation direction, giving rise to the phenomenon of dancing beamlets. Once the filaments propagate far enough away from this region, the light and density become sufficiently decorrelated that the interactions between light and plasma become nonlocal in both space and time. This results in more self-similar transient behavior which characterizes region III. Thus, time dependent filamentation and the accompanying SBFS persist for times long compared to global hydrodynamic times or typical laser pulse widths in ICF plasmas. We conclude that time dependent nonlocal behavior is the canonical feature of filamentation and SBFS in plasmas.

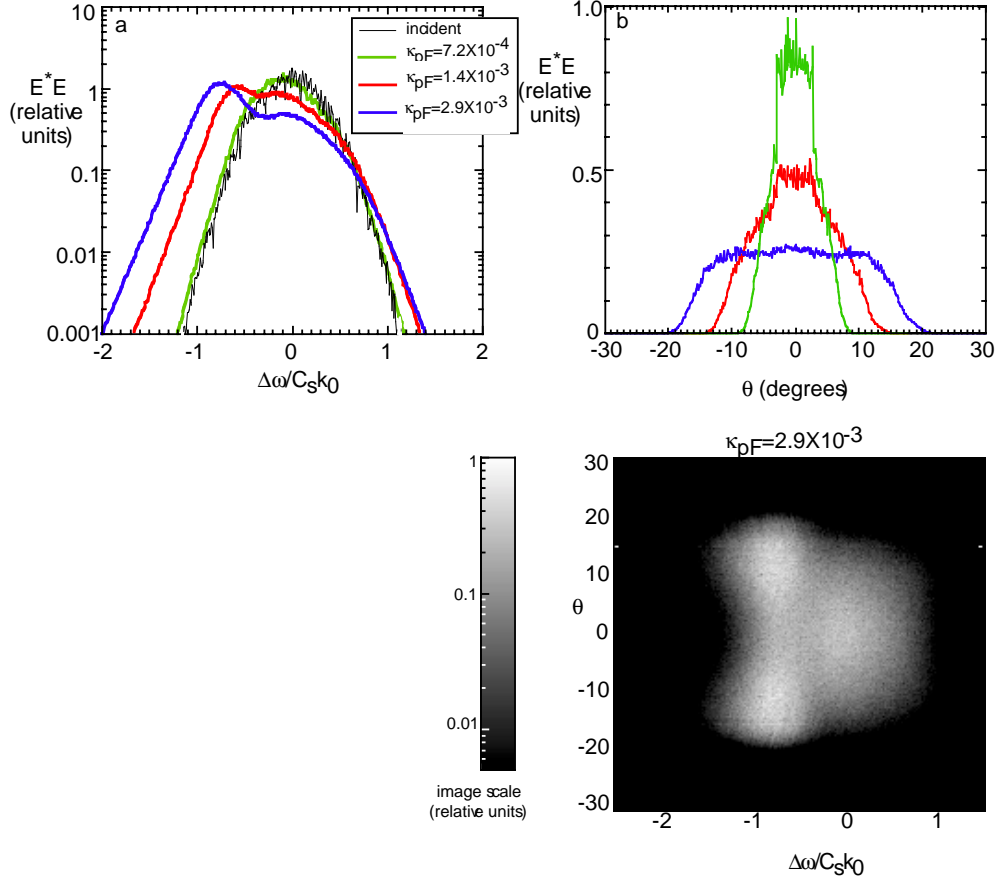


Figure 16: Results of simulations of interactions with an incident ISI beam, with all other conditions the same as in Fig. 1. The interaction strengths here are given by varying the intensity from  $2 - 6 \times 10^{15} W/cm^2$ . In all cases, the incident coherence time of the laser was  $\lambda_0/c_s$ , or about 0.8 psec. The (a) transmitted spectra, (b) transmitted angular light distribution, and (c) transmitted spectrum vs. angle for the most intense case  $\kappa_{pF} = 2.9 \times 10^{-3}$  are shown.

The amount of bandwidth and spatial incoherence impressed is proportional to the filamentation interaction strength. The power spectra of the transmitted light have broadened and red-shifted features, both of which increase as the interaction strength increases. The broadened spectrum also carries a distinctly red-shifted feature whose variation with angle is consistent with SBFS theory presented here.

The spatial incoherence impressed upon the laser can produce a much broader angular spread than that given by incident TBS optics. The spread is also larger than that predicted by steady state filamentation theory. This suggests that more than filamentation may be causing the beam to spread. Examination of the frequency and wavenumber spectra of the transmitted light, particularly the asymmetric wavelength shift and its dependence upon angle, reveals that SBFS is a contributing source to this additional spreading.

For interaction strengths that are largest, the induced bandwidth can rival the incident bandwidth from TBS optical smoothing methods such as ISI or SSD. At the same time, and in contrast to TBS, this induced angular spreading produces light far outside the cone of the incident optics. These features could be beneficial (the shorter speckle pattern in the plasma would help further reduce other instabilities, while the induced bandwidth minimizes the plasma response to local intensity hot spots) or they could be a hindrance (it would be harder to localize the deposited energy in a wildly spraying beam).

We remark on three important caveats concerning the present study. First, the modeling of the light is based on the spatially parabolic wave equation, which assumes that light travels mainly in the forward ( $\theta=0$ ) direction. For some of the simulations at the highest interaction strengths, this approximation (and the results) may be invalid (some light propagating at angles as high as 22 degrees from forward are seen). It is perhaps unfortunate that this approximation does not trigger violent behavior so as to signal its breakdown, when it occurs. We intend to remedy this weakness of PONHF2D by adopting a temporally enveloped but otherwise unapproximated wave equation model next.

We also note that these results have been obtained in the absence of all other laser-plasma instabilities, such as SRS or backwards SBS. If these other instabilities could prevent the first-foci of the filaments which these simulations reached before entering into the transition region (region II) and beyond, by significantly depleting the power in the filament, then they could well prevent the effects observed and reported here. For instance, in the complementary regime of single hot spot simulations, strong evidence exists that the evolution of filamentation, SBFS, and stimulated Brillouin backscattering (SBBS) can be interdependent[7]. We believe that this would also be the case in large scale simulations such as those presented here if SBBS were to be properly included. This analysis is outside the scope of the current study, but is a critical point that must be investigated further.

In addition, external plasma conditions such as flow inhomogeneities due to other laser beams illuminating the plasma and ion wave frequency modulations due to intensity variations caused by filamentation[30] can degrade the gain of SBFS, implying that the levels found in our present simulation may be overestimated. We plan to include these effects and assess their impact on SBFS and filamentation in future work.

We anticipate that for a laser such as the NIF, having external smoothing capability such as a few Angstroms of SSD would be a crucial step to avoid the unpredictable or unwarranted angular spreading and temporally unsteady behavior reported in this paper. In addition, however, for NIF class lasers, it is important to study the effects of multiple crossing beams on filamentation itself and on other instabilities, before having a more complete picture of the plasma physics issues that may be acute in such settings.

## 5 Acknowledgments

We would like to thank Bill Kruer, Steve Bodner, Tudor Johnston, Dave Montgomery, John Moody, John Gardner, and Robert Kirkwood for helpful discussions and comments regarding this paper. This work was supported by U.S. Department of Energy. B.B.A.'s work was performed under the auspices of the U.S. DoE by LLNL under contract No. W-7405-ENG-48.

## References

- [1] Lindl, J., Phys. Plasmas **2**, 3933 (1995).

- [2] Verdon, C.P., Bull. Am. Phys. Soc. **38**, 2010 (1993); McCrory, R.L. and Verdon, C.P., “Computer modeling and simulation in inertial confinement fusion,” *International School of Plasma Physics Piero Caldirola: Inertial Confinement Fusion (1988)*, edited by A. Caruso and E. Sindoni (Editrice Compositori, Bologna, Italy, 1988), pp. 83–124.
- [3] Epstein, R.E., J. Appl Phys. **82**, 2123 (1997).
- [4] Kruer, W.L., “*The Physics of Laser Plasma Interactions*” (Addison-Wesley, Redwood City, CA, 1988).
- [5] Vu, H.X., Phys. Plasmas **4**, 1841 (1997); Eliseev, V.V., Ourdev, I., Rozmus, W., Tikhonchuk, V.T., Capjack, C.E., Young, P.E., *Ion Wave Response to Intense Laser Beams in Underdense Plasmas*, submitted to Phys. Plasmas (1997).
- [6] Hüller, S., Mounaix, Ph., and Pesme, D., Physica Scripta **T63**, 151 1996.
- [7] Hüller, S., Mounaix, Ph., Tikhonchuk, V.T., and Pesme, D., Phys. Plasmas **4**, 2670 (1997); Eliseev, V.V., Rozmus, W., Tikhonchuk, V.T., and Capjack, C.E., Phys. Plasmas **3**, 2215 (1996).
- [8] Kaw, P., Schmidt, G. and Wilcox, T., Phys.Fl **16**, 1522 (1973); Max, C.E., Arons, J., Langdon, A. B., Phys. Rev. Lett. **33**, 209 (1974); Lam, J.F., Lippmann, B. and Tappert, F., Phys. Fluids **20**, 1176 (1977); Anderson, D. and Bonnedal, M., Phys. Fluids **22**, 105 (1979).
- [9] Milroy, R.D., Capjack, C.E., McMullin, J.N. and James, C.R., Can. J. Phys **57**, 514 (1979); Kane, E. and Hora, H., Aust. J. Phys **34**, 385 (1981); Schmitt, A.J. and Ong, R.S.B., J.Appl.Phys **54**, 3003 (1983); Rankin, R., Marchand, R. and Capjack, C.E., Phys. Fluids **31**, 2327 (1988).
- [10] Craxton, R.S. and McCrory, R.L., J. Appl. Phys. **56**, 108 (1984); Estabrook, K., Kruer, W.L. and Bailey, D.S., Phys. Fluids **28**, 19 (1985).
- [11] Schmitt, A.J., Phys. Fl **31**, 3079 (1988); Schmitt, A.J., Phys Fl. **B3**, 186 (1991).
- [12] Johnston, T.W., F. Vidal, and D. Frechette, Phys. Plasmas **4**, 1582 (1997).
- [13] Berger, R.L., Lasinski, B.F., Kaiser, T.B., Williams, E.A., Langdon, A.B. and Cohen, B.I., Phys. Fluids B **5**, 2243 (1993).
- [14] DeVore, C.R., J. Comp. Phys. **92**, 142 (1991); J. P. Boris and D. L. Book, J. of Comp. Phys. **20**, 397 (1976).
- [15] Valeo, E., Phys. Fluids **17**, 1391 (1974); Valeo, E. and Estabrook, K., Phys. Rev. Lett. **34**, 1008 (1975).
- [16] Coggeshall, S.V., Mead, W.C. and Jones, R.D., Phys. Fluids **31**, 2750 (1988).
- [17] Afeyan, B.B., Chou, A.E., Kirkwood, R.K., Kruer W.L., and Montgomery, D.S., *The Effect of Velocity Fluctuations and Laser Nonuniformities on Parametric Instabilities in Laser-Produced Plasmas*, submitted to Phys. of Plasmas (1997).
- [18] Lehmborg, R.H., Obenschain, S.P., Opt. Comm **46**, 27 (1983).
- [19] Skupsky, S., Short, R.W., Kessler, T., Craxton, R.S., Letzring, S. and Soures, J.M., J. Appl. Phys. **66**, 3456 (1989).
- [20] Fleck, J.A., Morris, J.R. and Feit, M.D., Applied Physics **10**, 129 (1976); Feit, M.D. and Fleck, J.A., J. Opt. Soc. Am. B **5**, 633 (1988).
- [21] Rose, H.A., Phys. Plasmas **3**, 1709 (1996).



- [22] Kruer, W.L., and Hammer, J.H., Comm. Plasma Phys. Cont. Fusion, **18**, 85 (1997); Moody, J.D., MacGowan, B.J., Hinkel, D.E., Kruer, W.L., Williams, E.A., Estabrook, K., Berger, R.L., Kirkwood, R.K., Montgomery, D.S., and Shepard, T.D., Phys. Rev. Lett. **77**, 1294 (1996); and Hinkel, D., Williams, E.A., and Still B., Phys. Rev. Lett. **77**, 1298 (1996).
- [23] Kato, Y. and Mima, K., Appl. Physics **B29**, 186 (1982).
- [24] S.N. Dixit, J.K. Lawson, K.R. Manes, H.T. Powell and K.A. Nugent, Optics Letters, **19**, 417, 1994.
- [25] In the notation of the papers[11],  $\kappa_{pF} \equiv (n_e/n_{crit})\gamma_p$ .
- [26] Wilks, S.C., Young, P.E., Hammer, J.M., Tabak, M., and Kruer, W.L., Phys. Rev. Lett. **73**, 2994 (1994).
- [27] Zakharov, V.E., Sov. Phys. JETP, **26**, 994 (1968); Zakharov, V.E., Sobolev, V.V., and Synakh, V.C., Sov. Phys. JETP, **33**, 77 (1971); Zakharov, V.E., and Rubenchik, A.M., Sov. Phys. JETP, **38**, 494 (1974).
- [28] Liu, C. S., and Kaw, P. K., "Parametric instabilities in homogeneous unmagnetized plasmas", in *Advances in Plasma Physics* Vol. 6, (A. Simon and W. Thompson, eds.) p.83-119, 1976.
- [29] Kruer, W.L., "Interaction Physics for MegaJoule Laser Fusion Targets" in *Laser Interaction and Related Plasma Phenomena* Vol. 10, (Plenum, NY 1992), pp. 503 – 509.
- [30] Afeyan, B.B., Chou, A.E., Matte, J.P., Town, R.P., Kruer, W.L., *Kinetic Theory of Electron Plasma and Ion Acoustic Waves in Nonuniformly Heated Laser-Plasmas*, submitted to Phys. Rev. Lett. (1997).